

# Catalytic properties of Cu–Mg–Al hydrotalcites, their oxides and reduced phases for ethanol dehydrogenation

Morgana Rosset<sup>1</sup> · Oscar W. Perez-Lopez<sup>1</sup>

Received: 4 September 2017 / Accepted: 23 October 2017 / Published online: 31 October 2017  
© Akadémiai Kiadó, Budapest, Hungary 2017

**Abstract** Different phases of Cu–Mg–Al compounds, hydrotalcites, their oxides, and reduced phases were prepared by co-precipitation and evaluated using the ethanol reactions. The solids were characterized by surface area measurements, X-ray diffraction (XRD), thermogravimetry coupled with differential thermal analysis, H<sub>2</sub>-temperature-programmed reduction, CO<sub>2</sub> temperature-programmed desorption and temperature-programmed oxidation. The catalytic runs were performed at temperatures ranging from 250 to 350 °C. Activation with H<sub>2</sub> was previously carried out in situ at 300 °C for the reduced samples. The samples with higher amount of Cu presented high ethanol conversion independent of the phase evaluated. The characterization by XRD after the reaction revealed that all samples exhibited only the metallic phase of Cu, independent of the phase before the reaction. The high selectivity for dehydrogenation was responsible for the transformation of hydrotalcites and mixed oxides into metallic phase during the ethanol reaction. Samples with lower amounts of Cu were deactivated by carbon deposition whereas samples with higher amount of Cu were deactivated mainly by sintering.

**Keywords** Hydrotalcites · Mixed oxides · Metallic phase · Cu–Mg–Al catalysts · Ethanol reactions

---

**Electronic supplementary material** The online version of this article (doi:[10.1007/s11144-017-1297-5](https://doi.org/10.1007/s11144-017-1297-5)) contains supplementary material, which is available to authorized users.

---

✉ Oscar W. Perez-Lopez  
perez@enq.ufrgs.br

Morgana Rosset  
morganar@enq.ufrgs.br

<sup>1</sup> Laboratory of Catalytic Processes-PROCAT, Department of Chemical Engineering, Federal University of Rio Grande do Sul (UFRGS), Rua Eng. Luiz Englert, s/n., Porto Alegre, RS CEP: 90040-040, Brazil

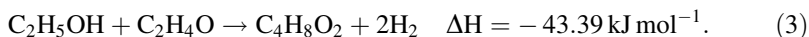
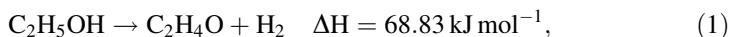
## Introduction

Layered double hydroxides (LDHs) are anionic clays, also known as hydrotalcite-like compounds, which have structures similar to brucite  $[\text{Mg}(\text{OH})_2]$ . The general formula for these compounds is  $[\text{M}_{1-x}^{2+}\text{M}_x^{3+}(\text{OH})_2]^{x+}\text{A}_{x/n}^{n-} \cdot y\text{H}_2\text{O}$ , where  $\text{M}^{2+}$  corresponds to bivalent and  $\text{M}^{3+}$  trivalent metallic cations,  $\text{A}^{n-}$  represents an inorganic or organic anion and  $x$  is the molar ratio of cations usually between  $0.20 \leq x \leq 0.33$  [1]. The combination and the ratio of metallic cations influence the structure and the chemical properties of LDH and mixed oxides [2]. LDHs are widely investigated due to their properties and potential applications as ion exchangers, adsorbents, catalysts, catalyst precursors and supports [3–10].

Thermal treatment of LDHs above a temperature of 350 °C causes the collapse of the lamellar structure which results in the formation of mixed metal oxides [11]. The structure and the catalytic properties after calcination depends on the chemical composition of the LDH precursor, temperature, and atmosphere during calcination [12, 13]. The mixed oxides derived from LDHs exhibit properties such as high surface area and porosity, thermal stability, good homogeneity, and high dispersion of metals [1].

The mixed oxides obtained from LDHs have shown great performance in numerous reactions of industrial interest such as reforming reactions of ethanol [14], methanol [15] and methane [16, 17]; Fischer–Tropsch synthesis [18]; selective oxidation of ammonia to dinitrogen [19]; and ethanol decomposition [20, 21].

The ethanol dehydrogenation to acetaldehyde (Eq. 1) is favored thermodynamically at high temperatures. The dehydrogenation of ethanol can also produce ethyl acetate (Eq. 2). On the other hand, the formation of ethyl acetate according to Eq. 3 is favored thermodynamically by low temperatures. The formation of ethyl acetate by Eq. 3 is the consequence of two consecutive reactions, with the production of acetaldehyde as intermediate step [22].



Catalysts containing copper were reported to be highly active and stable in methane oxidation reactions. Their activities depend on the copper content and the pH of coprecipitation [23]. Copper based catalysts also have been successfully employed for the selective conversion of ethanol to ethyl acetate and acetaldehyde [24], and for the hydroxylation of phenol [25].

Ethanol reactions performed using mixed oxide catalysts has been widely applied for the production of chemicals such as ethylene, hydrogen, diethyl ether, acetaldehyde, ethyl acetate, *n*-butanol and derivatives [26–30]. The selectivity of the products depends directly on the acid–base nature of the catalysts. Catalysts with acidic property have high selectivity for the ethanol dehydration, whereas the basic catalysts favor the dehydrogenation of ethanol [31, 32].

In this context, this work presents the synthesis, characterization and catalytic evaluation of Cu–Mg–Al LDHs, their mixed oxides resulting from calcination, as well as the metallic phases obtained after reduction. The catalytic activity of these different phases was evaluated using the ethanol reactions. To the best of our knowledge, this is the first report on the simultaneous evaluation of catalytic activity for the different phases of Cu–Mg–Al (hydrotalcites, mixed oxides and metallic phases).

## Experimental

### Catalysts preparation

The samples were synthesized through continuous co-precipitation following the previously described procedure [33, 34]. Two aqueous solutions were prepared: solution A containing a mixture of metal salts  $\text{Cu}(\text{NO}_3)_2$ ,  $\text{Mg}(\text{NO}_3)_2$  and  $\text{Al}(\text{NO}_3)_3$ ; solution B containing the precipitant  $\text{Na}_2\text{CO}_3$ . The atomic ratio of cations  $\text{M}^{2+}/\text{M}^{3+}$  was fixed at 4, while the atomic ratio  $\text{Mg}/\text{Cu}$  was between 1 and 3. The co-precipitation was conducted in a glass continuous stirred-tank reactor at a constant temperature (50 °C). The solution A was added at a constant flow rate, while the flow of the solution B was continuously adjusted to maintain the pH at a constant value ( $8 \pm 0.1$ ).

After the co-precipitation, the resulting material was collected and maintained under agitation for crystallization at 50 °C for 1 h and afterwards it was filtered and washed with deionized water. The slurry was dried at 80 °C for 12 h in an oven. The calcined samples were obtained by thermal treatment under air flow rate of  $50 \text{ mL min}^{-1}$  at 400 °C for 12 h.

### Catalysts characterization

The catalysts were characterized by X-ray diffractometry (XRD), BET surface area, thermogravimetry coupled with differential thermal analysis (TG–DTA),  $\text{CO}_2$  temperature-programmed desorption ( $\text{CO}_2$ -TPD), and temperature-programmed reduction ( $\text{H}_2$ -TPR). X-ray diffraction (XRD) and temperature-programmed oxidation (TPO) were used to characterize carbon deposited on the catalyst after of the ethanol reaction.

The surface area measurements of hydrotalcites and calcined samples were conducted using the conventional  $\text{N}_2$  adsorption/desorption on a Quantachrome Nova-1200 surface area analyzer at liquid nitrogen temperature. The samples were pretreated at 250 °C under a flow rate of  $30 \text{ mL min}^{-1}$  of He before the measurements. The specific surface areas were calculated using BET method ( $S_{\text{BET}}$ ).

The XRD patterns were collected through the powder method with a Bruker D2-Phaser diffractometer using  $\text{Cu K}\alpha$  radiation ( $\lambda = 1.5406 \text{ \AA}$ ) at 30 kV and 10 mA. The average crystallite sizes were determined by the Scherrer equation.

The thermal analysis of the hydrotalcites was performed by thermogravimetry (TG–DTA) using a TA thermobalance (Model SDT600). The samples were heated in the temperature range of 20–1000 °C at 10 °C min<sup>-1</sup> under an air flow rate of 100 mL min<sup>-1</sup>.

The TPR (H<sub>2</sub>-TPR) profiles were obtained using a multipurpose system (SAMP3) with a heating rate of 10 °C min<sup>-1</sup> up to 600 °C, using 30 mL min<sup>-1</sup> of a mixture 10% H<sub>2</sub>/N<sub>2</sub> (v/v). The data were recorded by a thermal conductivity detector.

To obtain the profiles of CO<sub>2</sub>-TPD, samples were pretreated under He flow 30 mL min<sup>-1</sup> at 100 °C. After that, the catalyst was saturated with CO<sub>2</sub> (30 mL min<sup>-1</sup>) for 1 h at 100 °C. The desorption of CO<sub>2</sub> was conducted by heating the sample at 10 °C min<sup>-1</sup> up to 600 °C, under He flow 30 mL min<sup>-1</sup>. The desorption profiles were deconvoluted using Gaussian curves in order to quantify basic sites.

The TPO analyses were performed using a TA SDT600 thermobalance. The samples were heated at 10 °C min<sup>-1</sup> from room temperature up to 600 °C under an air flow rate of 100 mL min<sup>-1</sup>.

## Catalytic activity

The catalytic activity for all the samples (hydrotalcites, calcined and reduced) was evaluated by the ethanol reaction. The activity tests were conducted in a fixed-bed quartz reactor loaded with 200 mg of sample, under atmospheric pressure at temperature between 250 and 350 °C. Nitrogen and ethanol were fed with a flow of 100 mL min<sup>-1</sup> and 0.4 mL h<sup>-1</sup>, respectively. For the reduced samples, the reduction was previously carried out in situ at 300 °C during 1 h under a flow of H<sub>2</sub> of 10 mL min<sup>-1</sup> and of N<sub>2</sub> of 100 mL min<sup>-1</sup>. The products were analyzed using an on-line Varian 3600CX gas chromatograph with a Porapak Q column and flame ionization detectors.

## Results and discussion

### Catalysts characterization

The nominal composition, the intended Mg/Cu ratio and the BET specific surface area for the prepared samples are listed in Table 1. The samples have been named as

**Table 1** Nominal compositions and BET surface areas for the hydrotalcites and calcined samples

Sample	Composition (atomic ratio) Cu/Mg/Al	Mg/Cu ratio	S <sub>BET</sub> (m <sup>2</sup> g <sup>-1</sup> )
HT-Cu20	20/60/20	3	81
HT-Cu40	40/40/20	1	52
C-Cu20	20/60/20	3	90
C-Cu40	40/40/20	1	53

HT-CuX (hydrotalcite), C-CuX (calcined) and R-CuX (reduced), where X represent the mol% of copper.

As seen in Table 1, the specific surface area increases when the Mg/Cu ratio increases from 1 to 3, for both hydrotalcites and calcined samples, demonstrating that Mg plays the role of structural promoter. On the other hand, comparing the hydrotalcites and the calcined samples, slightly larger surface areas for the calcined samples were observed, which is in agreement with the results in [35, 36].

The TG–DTA profiles are present in Fig. 1. It was observed that all the samples showed endothermic decomposition in two stages, in agreement with typical results for hydrotalcites [37, 38].

The first step in the range of 100–200 °C had a weight loss of approximately 14%, which can be attributed to the elimination of the interlayer water, resulting in the desorption of  $\text{OH}^-$  ions. The second thermal decomposition occurred at a temperature range between 500 and 700 °C. The weight loss in this stage is due to the dehydroxylation and anion carbonates decomposition. Chmielarz et al. [39] suggest that the introduction of Cu in the hydrotalcite structure stabilizes the carbonate anions, which are decomposed at higher temperature.

The weight losses for HT-Cu20 and HT-Cu40 catalysts were 40 and 35%, respectively. The sample with higher Mg content had a more accentuated weight loss indicating improved structural organization of hydroxycarbonates. In addition, the temperature for complete decomposition was in the same order: HT-Cu20 > HT-Cu40, indicating that the thermal stability decreases in the same trend.

The X-ray diffractograms of the Cu–Mg–Al hydrotalcites, calcined samples and reduced samples with different Mg/Cu ratios are showed in Fig. 2. The cell parameter of HT-Cu hydrotalcites phase was calculated assuming a 3R polytype with a hexagonal cell. The lattice parameters ( $a$  and  $c$ ), as well as the crystallite size are reported in Table 2.

It can be observed (Fig. 2) that all the uncalcined samples presented reflections at angles 11.7°, 23°, 34.5°, 60° and 62° in the crystalline planes of (003), (006), (012), (110) and (113) [40, 41], which corresponds to the hydrotalcite structure (JCPDS

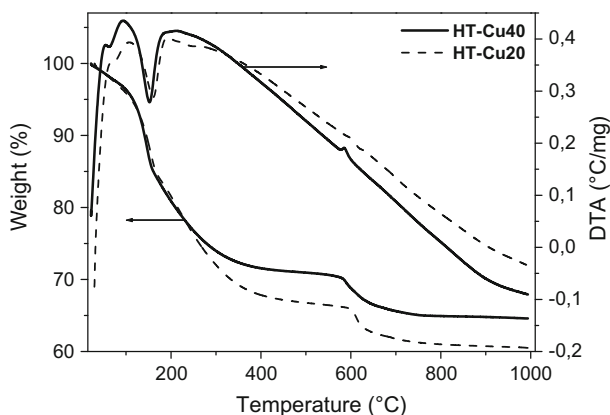


**Fig. 1** Thermogravimetric profile of the hydrotalcites: TG–DTA

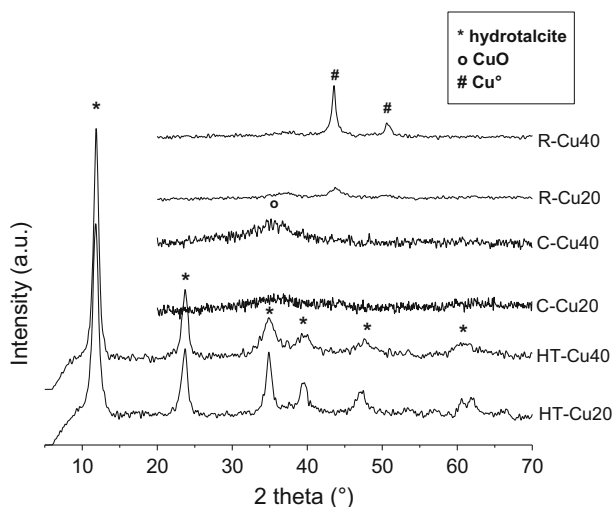


**Fig. 2** X-ray diffraction patterns for the samples before reaction: hydrotalcites, calcined samples at 400 °C and reduced samples at 300 °C

**Table 2** Lattice parameters for hydrotalcites and crystallite sizes for the catalysts before and after the ethanol reactions between 250 and 350 °C

Samples	Crystallite size (nm)		Lattice parameters	
	Before reaction	After reaction	<i>a</i> (Å)	<i>c</i> (Å)
HT-Cu20	10.2	9.2	3.056	22.52
HT-Cu40	11.8	14.7	3.062	22.37
C-Cu20	n.d.	10.7		
C-Cu40	n.d.	15.0		
R-Cu20	7.6	10.1		
R-Cu40	14.6	14.4		

41-1428). With the increase of the Cu content, a decrease in the sharpness of reflections at 60° and 62° was noticed. This is expected, since at higher concentrations of Cu a Jahn–Teller distortion occurs, leading to poor long range ordering [1]. The parameter *a* increases slightly with the increase of Cu content. The parameter *c* decreased with increasing Cu content, which indicates that the intercalation distance was reduced by the introduction of Cu in the hydrotalcite structure. In addition, the crystallite size increases as the amount of Cu increases (Table 2). The reflection at 11° was used to estimate the size of crystallites.

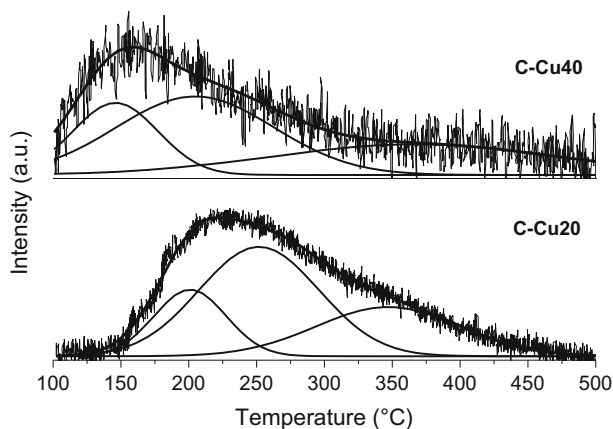
The XRD patterns for the calcined samples (Fig. 2) reveal poorly crystallized samples and indicating a very small crystallite size. The diffractograms present a broad reflection of low intensity at approximately 36° that may be related to CuO (JCPDS 48-1548). The characteristic reflections of hydrotalcites disappeared in all samples after calcination, indicating that the thermal treatment at 400 °C promotes the collapse and the decomposition of the hydrotalcite structure [42].

The XRD patterns for the reduced samples in Fig. 2 exhibit reflections at  $43^\circ$  and  $50^\circ$  which correspond to  $\text{Cu}^0$  phase (JCPDS 04-0836). These results proved that reducing conditions were sufficient to convert completely the oxides phases to the metallic phase. In addition, the sample with the higher Cu content showed more intense and sharp diffraction peaks; consequently, exhibiting the higher crystallite size, as shown in Table 2. The R-Cu40 sample with higher amount of Cu displayed sharper reflections than sample R-Cu20 that has lower amount of Cu. The crystallite size for reduced samples corroborated the great difference between these two samples resulting in crystallite sizes of 7.6 and 14.6 nm for R-Cu20 and R-Cu40, respectively (Table 2). This difference was also observed in the uncalcined samples, although to a lesser extent.

$\text{CO}_2$ -TPD profiles of the calcined samples are shown in Fig. 3. These profiles were deconvoluted in three desorption peaks. The weak strength sites are related for temperature lower than  $200^\circ\text{C}$ . Peaks between  $200$  and  $280^\circ\text{C}$  are assigned to medium strength basic sites, and for temperatures above  $300^\circ\text{C}$  to strong basic sites [28, 43]. Table 3 shows the quantification of the basic sites from deconvolution of  $\text{CO}_2$ -TPD profiles. The amount of basic sites decreased with the increase in Cu content. This decrease is related to the decrease of sites of medium and high strength. These results showed that the amount and the strength of the basic sites can be controlled varying the Cu/Mg ratio. This behavior was also reported by Marcu et al. and Zeng et al. [28, 44].

The TPR was performed to determine the reducibility of different species of Cu. The  $\text{H}_2$ -TPR profiles of Cu–Mg–Al oxides are shown in Fig. 4. Two hydrogen consumption peaks were observed, indicating different kinds of Cu species. The first peak can be ascribed to reduction of  $\text{Cu}^{2+}$  ions in lamellar structure and the second reduction peak can be related to CuO species with a strong interaction with the surface of Mg–Al mixed oxides [45].

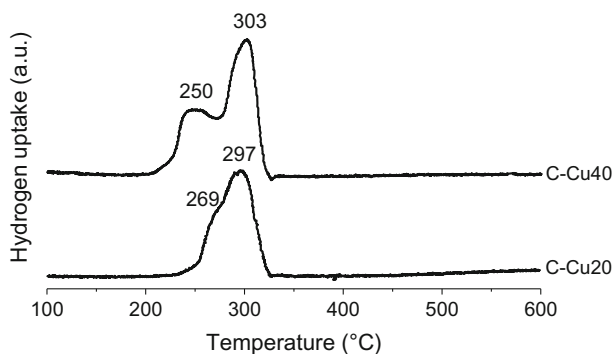
The first reduction peak shifted to lower temperatures with the increase in the amount of Cu. This indicates the reduction of further CuO particles with lower



**Fig. 3**  $\text{CO}_2$ -TPD profiles of the calcined samples at  $400^\circ\text{C}$

**Table 3** Density and strength of basic sites

Samples	Density of basic sites (mmol g <sup>-1</sup> )			
	Weak (%)	Medium (%)	Strong (%)	Total
C-Cu20	0.07 (19)	0.19 (52)	0.10 (29)	0.36
C-Cu40	0.03 (31)	0.04 (38)	0.03 (31)	0.10

**Fig. 4** H<sub>2</sub>-TPR profiles of samples calcined at 400 °C for 12 h

interaction, since the peak intensity also increases. In addition, the H<sub>2</sub> consumption increases by increasing the Cu content. These results indicate that the reduction temperature and the peak intensity are dependent on the Cu amount on sample.

### Catalytic activity

The catalytic activity for the different phases of Cu–Mg–Al compounds (hydrocalcite, calcined and reduced) was evaluated using the ethanol reactions temperatures between 250 and 350 °C. Table 4 summarizes the results of catalytic evaluation for all the samples. In this table, the ethanol conversion and the selectivity to the different products were compiled.

The hydrocalcites samples showed high activity even at low reaction temperatures. In the range between 250 and 300 °C, the catalytic activity was clearly related to the Cu amount in the sample. Thus, the HT-Cu40 sample presented the highest ethanol conversion. For temperatures higher than 300 °C, the ethanol conversion dropped for both samples indicating the catalyst deactivation. However, the deactivation was stronger for HT-Cu20 at 350 °C indicating a different mechanism of deactivation for both samples. Taking into account the size of crystallites after reaction for both samples (Table 2), the lower size for HT-Cu20 indicates that the deactivation for this sample was by carbon deposition, whereas for HT-Cu40 it was by sintering.

For the calcined samples no differences were found in ethanol conversions between 250 and 300 °C. Moreover, the sample with the higher Cu amount (C-Cu40) was more stable for temperatures above 300 °C, indicating better resistance to deactivation. Higher ethanol conversion for C-Cu40 at high temperatures can be



**Table 4** Conversion and selectivity as a function of reaction temperature for all the samples

Samples	T <sub>reac.</sub> (°C)	X <sub>EtOH</sub> (%)	S <sub>C2</sub> (%)	S <sub>AcH</sub> (%)	S <sub>PROP</sub> (%)	S <sub>BUT</sub> (%)	S <sub>EtOAc</sub> (%)	Others (%)
HT-Cu20	250	81.0	0.1	99.1	0.8	–	–	0.0
	275	94.2	0.3	97.2	2.0	0.1	0.4	0.1
	300	94.0	0.4	93.5	5.2	0.3	0.5	0.2
	325	78.0	0.7	93.6	1.0	1.4	3.1	0.1
	350	43.5	4.5	88.9	0.5	2.0	4.1	0.1
HT-Cu40	250	95.5	0.4	97.7	1.9	–	–	0.1
	275	97.8	0.8	92.3	2.7	1.0	2.8	0.4
	300	97.0	1.1	88.6	1.4	3.0	5.1	0.8
	325	78.9	4.3	81.1	0.7	3.7	6.4	3.8
	350	61.6	9.3	71.6	0.5	3.5	3.5	11.6
C-Cu20	250	89.5	0.1	90.4	3.6	1.6	4.3	0.0
	275	96.1	0.4	92.3	3.6	1.0	2.6	0.2
	300	96.8	0.5	91.6	3.9	1.5	2.3	0.3
	325	80.8	0.5	88.6	2.5	3.0	5.1	0.3
	350	49.7	5.0	82.4	0.9	4.9	5.8	1.0
C-Cu40	250	86.9	0.2	87.7	4.6	1.5	6.0	0.0
	275	95.6	0.7	87.1	4.2	2.2	5.6	0.2
	300	97.9	0.9	88.3	3.3	2.0	5.1	0.4
	325	95.6	1.0	86.2	2.3	3.2	6.8	0.5
	350	75.4	4.2	78.1	1.8	4.1	9.3	2.5
R-Cu20	250	78.7	0.1	94.6	0.6	1.8	2.9	0.0
	275	89.7	0.2	92.1	3.0	1.6	2.9	0.1
	300	89.7	0.3	92.1	2.2	1.9	3.4	0.1
	325	68.6	1.0	88.9	1.0	2.8	6.0	0.3
	350	40.8	7.6	79.4	0.0	5.0	4.3	3.6
R-Cu40	250	82.0	0.2	87.0	3.5	1.1	8.2	0.0
	275	95.8	0.4	87.8	2.6	2.2	6.9	0.1
	300	97.3	0.7	88.7	2.8	2.6	5.1	0.2
	325	94.3	1.1	84.7	3.5	3.7	5.7	1.2
	350	75.4	3.9	78.4	2.3	3.9	5.6	5.9

Others C<sub>3</sub>, C<sub>4</sub> and ethyl ether, XEtOH ethanol conversion, C2 ethylene, AcH acetaldehyde, PROP propanone, BUT butyraldehyde, EtOAc ethyl acetate

related to the excess copper in this sample. Nevertheless, the size of crystallites after the reaction for C-Cu40 sample was higher than that of C-Cu20 (Table 2). This suggests that the decrease in the ethanol conversion for C-Cu40 sample at high temperatures is due to the agglomeration of Cu particles. The deactivation at higher temperatures for samples with less Cu (C-Cu20) can be ascribed to carbon deposition rather than sintering.

For the samples that were reduced previously in  $H_2$ , both samples showed similar ethanol conversion at 250 °C. However, the difference in activity between the samples also increases as the temperature increases. Thus, the largest difference in ethanol conversion was observed at the highest temperature. Among the two samples, R-Cu40 presented the higher conversion in the whole range of temperature. In addition, this sample also shows higher stability, and thus better resistance to deactivation.

As can be seen (Table 4), acetaldehyde was the main product of the reaction resulting from the ethanol dehydrogenation. A high selectivity to this product was obtained for all the samples, ranging between 70 and 99%. Other products were ethylene, propanone, ethyl acetate and butyraldehyde, similar to the obtained in [22, 26, 46].

Regarding the selectivity for ethylene and acetaldehyde, an opposite behavior was observed with increasing temperature. The selectivity for ethylene increases with the increase of the reaction temperature as a result of the endothermic nature of the dehydration reaction. The selectivity for acetaldehyde was highest at the lower reaction temperatures, higher than 99% at 250 °C for HT-Cu20, although it decreases with the increase in temperature to around 72% at 350 °C for HT-Cu40 sample.

The selectivity for ethyl acetate did not show a clear trend with respect to the reaction temperature. Among the samples, the catalysts with the higher Cu content, namely: HT-Cu40, C-Cu40 and R-Cu40 were those that provided the highest selectivity to ethyl acetate of about 6, 9, and 8%. It is important to mention that the increase in the selectivity to ethyl acetate is related to the decrease of acetaldehyde, which is apparently consumed for the formation of ethyl acetate, in agreement with reaction represented by Eq. 3. According to Carotenuto et al. [22], the rate determining step should be the dual sites reaction between two adsorbed molecules of ethanol and acetaldehyde to give adsorbed ethyl acetate and hydrogen.

From the examination of the selectivity for butyraldehyde, it can be observed that it increases as the temperature rises. Among the hydrotalcites, the sample that exhibited the highest selectivity for butyraldehyde was HT-Cu40. On the other hand, the calcined samples showed no significant differences of selectivity for butyraldehyde between them.

### Characterization of the spent catalysts

Interestingly, the XRD patterns for hydrotalcites after the ethanol reaction in Fig. 5 showed only reflections assigned to  $Cu^0$  (JCPDS 4-0836) and  $Cu_2O$  (JCPDS 5-0667) phases, revealing the destruction of the LDH structure of these samples during the reaction. The formation of Cu metallic phase can be ascribed to the reducing atmosphere. This is due to the presence of  $H_2$  in large amount as the product of ethanol dehydrogenation, since the selectivity for acetaldehyde was high for both samples, around 98% at 250 °C (Table 4).

The diffractograms for the calcined samples (Fig. 5) mainly showed reflections at 43.3° and 50.4° ascribed to the copper metallic. The sample C-Cu40 also shows a reflection at 36.7° corresponding to  $Cu_2O$ , as residual of the oxides phases [47]. In

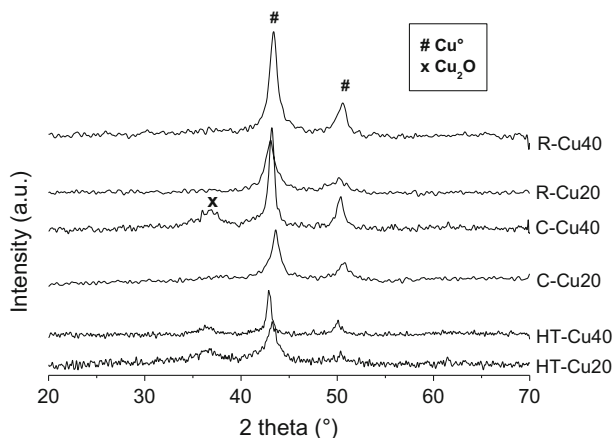


**Fig. 5** X-ray patterns of the samples after the ethanol reactions between 250 and 350 °C: hydrotalcites, calcined samples at and reduced samples

addition, it can be noticed that sample with higher Cu content (C-Cu40) exhibited sharper reflections than that of C-Cu20, indicating crystallites with larger size, in agreement with the results obtained by the Scherrer equation (Table 2).

The XRD pattern after the reaction for previously reduced samples in Fig. 5 showed only diffraction peaks of  $\text{Cu}^0$  phase. The R-Cu40 sample exhibited stronger reflections compared to R-Cu20 due to higher relative amount of Cu on R-Cu40. So, if the crystallite size for these samples (Table 2) are compared before and after the reaction, it would be noticed that R-Cu40 has practically the same crystallite size before and after the reaction (approximately 14 nm), while the particle size increases from 7.6 nm before the reaction to 10.1 nm after the reaction for R-Cu20 sample. These results explain the great differences between previously reduced samples in the ethanol conversions obtained at higher temperatures (Table 4).

Fig. 6 shows the TPO profiles for the spent catalysts after the ethanol reactions. Due to the removal of volatile and easily oxidizable species, the TPO profile for HT-Cu40 sample showed a weight loss until around 150 °C. After that, a weight increase was observed between 150 and 350 °C which can be attributed to the oxidation of copper metallic particles still present after the reaction [33, 48]. On the other hand, sample HT-Cu20 shows a continuous weight loss. The weight loss between 200 and 450 °C reveals the oxidation of amorphous carbon deposited on the surface of the catalyst. This carbon may be responsible through the deactivation of this sample for reaction temperatures higher than 300 °C (Table 4). Taking into account that sample HT-Cu40 did not show carbon deposition in TPO profile, the deactivation for this sample at high reaction temperatures can be ascribed to the sintering of Cu particles, as shown in Table 2.

Both calcined samples showed a marked weight loss up to 250 °C. The C-Cu40 sample had slight weight increase above 250 °C, which corresponds to the oxidation of the metallic phase. However, considering the total weight loss, it can be seen that the carbon production was higher in sample C-Cu20.

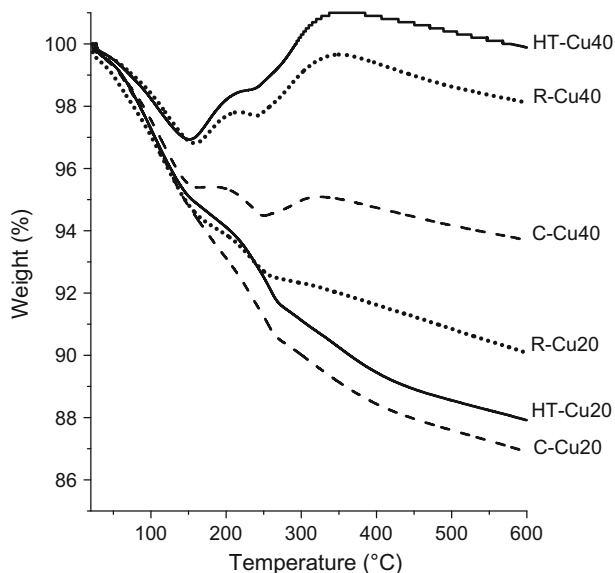


**Fig. 6** TPO profiles for samples after the ethanol reactions between 250 and 350 °C: hydrotalcites, calcined samples, and reduced samples

The highest weight loss was observed in R-Cu20, indicating a greater coke formation on this sample during the reaction. The R-Cu40 sample first showed a slight weight loss up to 150 °C due to the oxidation of volatile compounds, followed by a weight increase in two steps. The weight increase can be related to the oxidation of  $\text{Cu}^0$  derived from CuO at around 250 °C and to the oxidation of  $\text{Cu}^0$  with strong interaction with the mixed oxides at around 350 °C.

## Discussion

A large difference in surface area was observed for both hydrotalcites and oxides samples while comparing samples with different compositions (different Mg/Cu ratios). Samples with higher Mg/Cu ratio (lower amount of Cu) provided solids with higher specific surface area. These results are in agreement with those found by Basag et al. [19], who obtained a BET surface area of  $239 \text{ m}^2 \text{ g}^{-1}$  for a sample with Mg/Cu = 12.4. This ratio is higher than those used in the present work. Nevertheless, the XRD patterns of the uncalcined and calcined samples were not significantly influenced by these differences. The uncalcined samples showed typical pattern of hydrotalcite-like compounds and both calcined samples showed similar XRD pattern, typical of poor crystalline oxides. More remarkable differences were observed in the XRD patterns of the reduced samples with different Mg/Cu ratio.

The catalytic activity results for the uncalcined samples or hydrotalcites clearly show a strong deactivation at reaction temperatures higher than 300 °C. The deactivation was more marked for HT-Cu20. This behavior was surprising if the

crystallite size is considered, because the sample with the lower crystallite size (HT-Cu20) showed stronger deactivation than that with the greater crystallite size (HT-Cu40). The XRD patterns after the reaction showed a smaller crystallite size for HT-Cu20 whereas it was greater for HT-Cu40. This reveals that deactivation of HT-Cu20 was not due to the sintering. However, the TPO results showed a great formation of carbon on HT-Cu20, differently from sample HT-Cu40 where practically no carbon was formed. This demonstrates that the deactivation of HT-Cu20 was due to carbon deposition. Regarding HT-Cu40, although sintering occurred because its crystallite size increased after the reaction, this sample showed higher ethanol conversion than HT-Cu20 at 350 °C. This result can be ascribed to the larger amount of Cu present on HT-Cu40. From the TPR results, it can be inferred that Cu with low interaction undergoes sintering while Cu with strong interaction is preserved. Thus, the Cu phase with strong interaction would be responsible for the greater resistance to deactivation, avoiding the carbon deposition.

It is also clear that the differences in the catalytic activity for the hydrotalcites cannot be related to the specific surface area because the sample with the larger specific surface area is the sample with the lower amount of Cu (HT-Cu20), which presents lower activity compared to HT-Cu40 in the whole temperature range.

Another interesting result was the complete transformation of the double layered structure after the reaction in the metallic phase for uncalcined samples. The reaction temperatures used in the catalytic runs were probably responsible for the thermal decomposition of the hydrotalcites; however, the presence of metallic copper as the single phase in the spent samples would only be possible under reduction atmosphere. This condition was provided by the high selectivity for the dehydrogenation reaction [22], since the selectivity for acetaldehyde and consequently for hydrogen production was higher than 90%. According to Freitas et al. [46] the high selectivity to acetaldehyde can be associated with the presence of  $\text{Cu}^+$  species.

The results of ethanol conversion for the calcined samples were practically the same for both samples between the range 250 and 300 °C (Table 4). However, taking into consideration the amount of Cu on sample, we can say that HT-Cu20 sample is more active by unit of Cu. These results proved that the activity was independent of the surface area (90 and 53  $\text{m}^2 \text{g}^{-1}$  for C-Cu20 and C-Cu40, respectively). However, the differences in activity were more pronounced above 300 °C, since C-Cu20 showed lower conversions than C-Cu40 at higher temperatures. The XRD patterns of the spent samples showed more sharp reflections of  $\text{Cu}^0$  phase for C-Cu40, demonstrating the sintering on this sample as revealed by the crystallite size of 15 nm determined after the reaction (Table 2). On the other hand, the calcined samples showed remarkable differences in the carbon formation (Fig. 6), where sample C-Cu20 presented a great carbon amount in comparison with the C-Cu40 sample [49]. Therefore, it is very reasonable to suppose that the deactivation of C-Cu20 is due to the carbon deposition and more specifically to the carbon encapsulation, because the crystallite size after the reaction for this sample was 10.7 nm. Conversely, considering that the sample with the high amount of Cu (C-Cu40) presented a higher crystallite size, the deactivation of this sample would

be related mostly to the sintering of  $\text{Cu}^0$  rather than carbon deposition. Also, by taking into account the activity differences at higher temperatures, it can be said that the deactivation by carbon deposition have greater effect on the catalyst activity than sintering.

The XRD pattern for R-Cu40 showed sharps reflections of  $\text{Cu}^0$  phase than for R-Cu20 sample. The crystallite size for R-Cu40 was approximately twice of R-Cu20 as shown in Table 2 (14.6 and 7.6 nm). These results are in agreement with the TPR profiles, since R-Cu40 showed a low reduction temperature (250 °C) for the first peak. Taking into account that these samples were reduced at 300 °C before the reaction, a sintering of the CuO phase corresponding to the first peak in TPR is expected for sample R-Cu40. The deactivation by copper sintering has been reported in the literature [50, 51] due to its low thermal resistance. Interestingly, the crystallite size before and after the reaction was practically the same for R-Cu40, but different for R-Cu20 sample. In addition, for the whole temperature range, the ethanol conversion was higher for R-Cu40 compared to the R-Cu20 sample. The TPO profiles also revealed that R-Cu20 presented a higher carbon deposition compared to the R-Cu40 sample. These results explain the catalytic behavior of both samples, since R-Cu20 deactivated by carbon deposition combined with sintering. The results of ethanol conversion for the reduced samples also proved that the deactivation by coke deposition was more deleterious than sintering.

## Conclusion

The specific surface area for hydrotalcites and their oxides was strongly dependent on the amount of Cu in the sample. Samples with  $\text{Mg}/\text{Cu} = 3$  ratio showed higher surface area than samples with  $\text{Mg}/\text{Cu} = 1$ , independent of the samples being calcined or not.

The characterization by XRD showed LDH or hydrotalcite-like structure for uncalcined samples. These materials resulted in poor crystalline oxides after the thermal treatment. The reduced samples showed single  $\text{Cu}^0$  crystalline phase. The crystallite size for samples with the high amount of Cu ( $\text{Mg}/\text{Cu} = 1$ ) was higher than samples with  $\text{Mg}/\text{Cu} = 3$ .

The catalytic activity of uncalcined and calcined samples was independent of their specific surface area. The samples with higher amount of Cu presented high ethanol conversion, independent of the phase evaluated (uncalcined, calcined or reduced). These results were related to the excess Cu in the samples with  $\text{Mg}/\text{Cu} = 1$  ratio and to the lower carbon deposition on these samples. All the samples showed high selectivity for acetaldehyde as a product of ethanol dehydrogenation. The selectivity for acetaldehyde was higher at lower reaction temperatures.

The characterization after the reaction revealed that all the samples exhibited only the metallic phase of Cu in the XRD pattern, independent of the phase present before the reaction (hydrotalcites, oxides or metallic). The high selectivity for dehydrogenation was responsible for the transformation of hydrotalcites and mixed oxides into metallic phase during the ethanol reaction.

All samples showed deactivation to a greater or lesser extent for reaction temperatures higher than 300 °C. Samples with lower amount of Cu were deactivated by carbon deposition; whereas samples with higher amount of Cu were deactivated mainly by sintering. Samples with lower amount of Cu showed stronger deactivation than samples with higher Cu amount, suggesting that the carbon deposition was more deleterious than sintering. These results are supported by XRD and TPO characterization.

**Acknowledgements** The authors acknowledge CAPES for the financial support granted to carry out this work.

## References

1. Cavani F, Trifirò F, Vaccari A (1991) Hydrotalcite-type anionic clays: preparation, properties and applications. *Catal Today* 11(2):173–301
2. Reichle WT (1986) Synthesis of anionic clay minerals (mixed metal hydroxides, hydrotalcite). *Solid State Ion* 22(1):135–141
3. Vaccari A (1998) Preparation and catalytic properties of cationic and anionic clays. *Catal Today* 41(1–3):53–71
4. Ulbarri MA, Pavlovic I, Barriga C, Hermosín MC, Cornejo J (2001) Adsorption of anionic species on hydrotalcite-like compounds: effect of interlayer anion and crystallinity. *Appl Clay Sci* 18(1–2):17–27
5. Zhao R, Yin C, Zhao H, Liu C (2003) Synthesis, characterization, and application of hydrotalcites in hydrodesulfurization of FCC gasoline. *Fuel Process Technol* 81:201–209
6. Takehira K, Shishido T (2007) Preparation of supported metal catalysts starting from hydrotalcites as the precursors and their improvements by adopting “memory effect”. *Catal Surv Asia* 11(1–2):1–30
7. Guo Y, Zhu Z, Qiu Y, Zhao J (2013) Enhanced adsorption of acid brown 14 dye on calcined Mg/Fe layered double hydroxide with memory effect. *Chem Eng J* 219:69–77
8. Fan G, Li F, Evans DG, Duan X (2014) Catalytic applications of layered double hydroxides: recent advances and perspectives. *Chem Soc Rev* 43(20):7040–7066
9. Delidovich I, Palkovits R (2015) Structure-performance correlations of Mg–Al hydrotalcite catalysts for the isomerization of glucose into fructose. *J Catal* 327:1–9
10. Kubic D, Hájek M, Kutálek P, Smoláková L, Troppová I, Libor C (2015) Transesterification of rapeseed oil by Mg–Al mixed oxides with various Mg/Al molar ratio. *Chem Eng J* 263:160–167
11. Yang W, Kim Y, Liu PKT, Sahimi M, Tsotsis TT (2002) A study by in situ techniques of the thermal evolution of the structure of a Mg–Al–CO<sub>3</sub> layered double hydroxide. *Chem Eng Sci* 57(15):2945–2953
12. Rives V (2002) Characterisation of layered double hydroxides and their decomposition products. *Mater Chem Phys* 75:19–25
13. Jabłońska M, Chmielarz L, Węgrzyn A, Guzik K, Piwowarska Z, Witkowski S, Walton RI, Dunne PW, Kovanda F (2013) Thermal transformations of Cu–Mg (Zn)–Al(Fe) hydrotalcite-like materials into metal oxide systems and their catalytic activity in selective oxidation of ammonia to dinitrogen. *J Therm Anal Calorim* 114:731–747
14. Coleman LJI, Epling W, Hudgins RR, Croiset E (2009) Ni/Mg–Al mixed oxide catalyst for the steam reforming of ethanol. *Appl Catal A* 363(1–2):52–63
15. Hammoud D, Gennequin C, Aboukaï A, Abi AE (2014) Steam reforming of methanol over x% Cu/Zn–Al 400 500 based catalysts for production of hydrogen: preparation by adopting memory effect of hydrotalcite and behavior evaluation. *Int J Hydrog Energy* 40:1283–1297
16. González AR, Asencios YJO, Assaf EM, Assaf JM (2013) Dry reforming of methane on Ni–Mg–Al nano-spheroid oxide catalysts prepared by the sol–gel method from hydrotalcite-like precursors. *Appl Surf Sci* 280:876–887

17. Tanasoi S, Tanchoux N, Urdă A, Tichit D, Săndulescu I, Fajula F, Marcu IC (2009) New Cu-based mixed oxides obtained from LDH precursors, catalysts for methane total oxidation. *Appl Catal A* 363(1–2):135–142
18. Di Fronzo A, Pirola C, Comazzi A, Galli F, Bianchi CL, Di Michele A, Vivani R, Nocchetti M, Bastianini M, Boffito DC (2014) Co-based hydrotalcites as new catalysts for the Fischer–Tropsch synthesis process. *Fuel* 119:62–69
19. Basag S, Kocol K, Piwowarska Z, Rutkowska M, Baran R, Chmielarz L (2017) Activating effect of cerium in hydrotalcite derived Cu–Mg–Al catalysts for selective ammonia oxidation and the selective reduction of NO with ammonia. *Reac Kinet Mech Cat* 121:225–240
20. Carvalho DL, De Avillez RR, Rodrigues MT, Borges LEP, Appel LG (2012) Mg and Al mixed oxides and the synthesis of *n*-butanol from ethanol. *Appl Catal A* 415–416:96–100
21. Baylon RAL, Sun J, Wang Y (2014) Conversion of ethanol to 1,3-butadiene over Na doped Zn<sub>x</sub>Zr<sub>y</sub>O<sub>z</sub> mixed metal oxides. *Catal Today* 259:446–452
22. Carotenuto G, Tesser R, Di Serio M, Santacesaria E (2013) Kinetic study of ethanol dehydrogenation to ethyl acetate promoted by a copper/copper-chromite based catalyst. *Catal Today* 203:202–210
23. Răciulete M, Layrac G, Tichit D, Marcu IC (2014) Comparison of Cu<sub>x</sub>ZnAlO mixed oxide catalysts derived from multicationic and hybrid LDH precursors for methane total oxidation. *Appl Catal A* 477:195–204
24. Hosoglu F, Faye J, Mareseanu K, Tesquet G, Miquel P, Capron M, Gardoll O, Lamonnier JF, Lamonnier C, Dumeignil F (2015) High resolution NMR unraveling Cu substitution of Mg in hydrotalcites-ethanol reactivity. *Appl Catal A* 504:533–541
25. Kannan S, Dubey A, Knozinger H (2005) Synthesis and characterization of CuMgAl ternary hydrotalcites as catalysts for the hydroxylation of phenol. *J Catal* 231(2):381–392
26. Inui K, Kurabayashi T, Sato S, Ichikawa N (2004) Effective formation of ethyl acetate from ethanol over Cu–Zn–Zr–Al–O catalyst. *J Mol Catal A* 216(1):147–156
27. Varisli D, Dogu T, Dogu G (2007) Ethylene and diethyl-ether production by dehydration reaction of ethanol over different heteropolyacid catalysts. *Chem Eng* 62(18–20):5349–5352
28. Marcu IC, Tichit D, Fajula F, Tanchoux N (2009) Catalytic valorization of bioethanol over Cu–Mg–Al mixed oxide catalysts. *Catal Today* 147(3–4):231–238
29. León M, Díaz E, Ordóñez S (2011) Ethanol catalytic condensation over Mg–Al mixed oxides derived from hydrotalcites. *Catal Today* 164(1):436–442
30. Zonetti PC, Celnik J, Letichevsky S, Gaspar AB, Appel LG (2011) Chemicals from ethanol—the dehydrogenative route of the ethyl acetate one-pot synthesis. *J Mol Catal A* 334(1–2):29–34
31. Gines MJL, Iglesia E (1998) Bifunctional condensation reactions of alcohols on basic oxides modified by copper and potassium. *J Catal* 172:155–172
32. Phung TK, Busca G (2015) Diethyl ether cracking and ethanol dehydration: acid catalysis and reaction paths. *Chem Eng J* 272:92–101
33. Perez-Lopez OW, Senger A, Marcilio NR, Lansarin MA (2006) Effect of composition and thermal pretreatment on properties of Ni–Mg–Al catalysts for CO<sub>2</sub> reforming of methane. *Appl Catal A* 303:234–244
34. Escobar C, Perez-Lopez OW (2014) Hydrogen production by methane decomposition over Cu–Co–Al mixed oxides activated under reaction conditions. *Catal Lett* 144:796–804
35. Narasimharao K, Al-Sabban E, Saleh TS, Gallastegui AG, Sanfiz AC, Basahel S, Thabaiti A, Alyoubi A, Obaid A, Mokhtar M (2013) Microwave assisted efficient protocol for the classic Ullmann homocoupling reaction using Cu–Mg–Al hydrotalcite catalysts. *J Mol Catal A* 379:152–162
36. Genty E, Brunet J, Pequeux R, Capelle S, Siffert S, Cousin R (2016) Effect of Ce substituted hydrotalcite-derived mixed oxides on total catalytic oxidation of air pollutant. *Mater Today Proc* 3(2):277–281
37. Basag S, Piwowarska Z, Kowalczyk A, Wegrzyn A, Baran R, Gil B, Michalik M, Chmielarz L (2016) Cu–Mg–Al hydrotalcite-like materials as precursors of effective catalysts for selective oxidation of ammonia to dinitrogen—the influence of Mg/Al ratio and calcination temperature. *Appl Clay Sci* 129:122–130
38. Palacio LA, Velásquez J, Echavarría A, Faro A, Ribeiro FR, Ribeiro MF (2010) Total oxidation of toluene over calcined trimetallic hydrotalcites type catalysts. *J Hazard Mater* 177:407–413
39. Chmielarz L, Kuśtrowski P, Rafalska-Lasocha A, Majda D, Dziembaj R (2002) Catalytic activity of Co–Mg–Al, Cu–Mg–Al and Cu–Co–Mg–Al mixed oxides derived from hydrotalcites in SCR of NO with ammonia. *Appl Catal B* 35(3):195–210



40. Barrault J, Derouault A, Courtois G, Maissant JM, Dupin JC, Guimon C, Martinez H, Dumitriu E (2004) On the catalytic properties of mixed oxides obtained from the Cu–Mg–Al LDH precursors in the process of hydrogenation of the cinnamaldehyde. *Appl Catal A* 262(1):43–51
41. Thouchprasitchai N, Luengnaruemitchai A, Pongstabodee S (2016) The activities of Cu-based Mg–Al layered double oxide catalysts in the water gas shift reaction. *Int J Hydrog Energy* 41(32):14147–14159
42. Kovanda F, Jiráková K, Rymeš J, Koloušek D (2001) Characterization of activated Cu/Mg/Al hydrotalcites and their catalytic activity in toluene combustion. *Appl Clay Sci* 18(1–2):71–80
43. Di Cosimo JI, Díez VK, Xu M, Inglesia E, Apesteguía CR (1998) Structure and surface and catalytic properties of Mg–Al basic oxides. *J Catal* 178:499–510
44. Zeng Y, Zhang T, Xu Y, Ye T, Wang R, Yang Z, Jia Z, Ju S (2016) Cu/Mg/Al hydrotalcite-like hydroxide catalysts for *o*-phenylphenol synthesis. *Appl Clay Sci* 126:207–214
45. Yuan Z, Wang L, Wang J, Xia S, Chen P, Hou Z, Zheng X (2011) Hydrogenolysis of glycerol over homogeneously dispersed copper on solid base catalysts. *Appl Catal B* 101(3–4):431–440
46. Freitas IC, Damyanova S, Oliveira DC, Marques CMP, Bueno JMC (2014) Effect of Cu content on the surface and catalytic properties of Cu/ZrO<sub>2</sub> catalyst for ethanol dehydrogenation. *J Mol Catal A* 381:26–37
47. Auer SM, Gredig SV, Koppel RA, Baiker A (1999) Synthesis of methylamines from CO<sub>2</sub>, H<sub>2</sub> and NH<sub>3</sub> over Cu–Mg–Al mixed oxides. *J Mol Catal* 141:193–203
48. Hermes NA, Lansarin MA, Perez-Lopez OW (2011) Catalytic decomposition of methane over M–Co–Al catalysts (M = Mg, Ni, Zn, Cu). *Catal Lett* 141(7):1018–1025
49. Berndt FM, Perez-Lopez OW (2017) Catalytic decomposition of methane over Ni/SiO<sub>2</sub>: influence of Cu addition. *Reac Kinet Mech Cat* 120(1):181–193
50. Santacesaria E, Carotenuto G, Tesser R, Di Serio M (2012) Ethanol dehydrogenation to ethyl acetate by using copper and copper chromite catalysts. *Chem Eng J* 179:209–220
51. Thurgood CP, Amphlett JC, Mann RF, Peppley BA (2003) Deactivation of Cu/ZnO/Al<sub>2</sub>O<sub>3</sub> catalyst: evolution of site concentrations with time. *Top Catal* 22:253–259